Journal of Materials Chemistry C

Direct Solid-State Nucleation and Charge-Transport Dynamics of Alkali Metal-Intercalated $M_2Mo_6S_6$ (M = K, Rb, Cs) Nanorods

Journal:	*Journal of Materials Chemistry C*
Manuscript ID	TC-COM-04-2020-001674.R1
Article Type:	Communication
Date Submitted by the Author:	24-May-2020
Complete List of Authors:	Perryman, Joseph; University of California Davis, Department of Chemistry Kulkarni, Ambarish; University of California Davis Department of Chemical Engineering and Materials Science Velazquez, Jesus; University of California Davis, Department of Chemistry

COMMUNICATION

Direct Solid-State Nucleation and Charge-Transport Dynamics of Alkali Metal-Intercalated $M_2Mo_6S_6$ (M = K, Rb, Cs) Nanorods

Received 00th January 20xx,
Accepted 00th January 20xx

DOI: 10.1039/x0xx00000x

Joseph T. Perryman[a], Ambarish R. Kulkarni[b], and Jesús M. Velázquez*[a]

Microwave-assisted solid-state heating has been employed to control anisotropic growth of $M_2Mo_6S_6$ (M = K, Rb, Cs) pseudo-Chevrel Phase nanorods without a growth template for the first time. Pronounced preferential crystal nucleation along the hexagonal axis is observed, and electrochemical methods are employed to elucidate viability for employment of these materials in energy storage and energy conversion systems. It is observed that these nanomaterials exhibit moderate and under-explored capacitive behavior with charge storage capabilities ranging from 2-8 F/g in strongly acidic aqueous electrolyte, as well as promising electrochemical performance, evolving hydrogen gas at 10mA/cm^2 under an applied bias of less than 300mV vs RHE.

Molybdenum chalcogenides have attracted much attention over the years, owing to their compositional and dimensional tunability that engenders a wide range of favorable chemical and physical properties. Two-dimensional molybdenum chalcogenides in the MX_2 family (M = Mo, X = S, Se, Te) have attracted immense focus, due to their composition-dependent electronic structure,[1, 2] as well as the plethora of available synthetic methods with which researchers can achieve precise control of dopant density,[3, 4] heterostructure growth,[5-7] as well as layer-dependent properties where indirect-to-direct band-gap transitions have engendered uniquely controllable optical behavior.[8, 9]

Three-dimensional molybdenum chalcogenides such as the $M_yMo_6X_8$ (M= Alkali, Alkaline Earth, Transition, or Post-Transition Metals, y = 0-4, X = S, Se, Te) Chevrel-Phases (CPs) have been widely investigated as a result of their unique electronic and structural properties that lead to favorable performance in interfacial electron-transfer reactions like CO_2, CO, and H^+ reduction.[10, 11] In previous work, much promise has been attributed to CP chalcogenides owing to their favorably positioned Mo d-band and chalcogen p-band,[10, 12] which engender tunable small-molecule reduction reactivity and charge-transfer kinetics.[13] CPs have also been successfully integrated in energy storage devices where multivalent cations are intercalated and de-intercalated from the crystal lattice with impressively low coulombic restriction.[14-16] Furthermore, these ternary chalcogenides have found use in electronic devices where their thermoelectric and superconducting properties can be exploited.[17-19]

With this work we introduce a facile synthetic method which yields an analogous one-dimensional class of ternary chalcogenides with the composition $M_2Mo_6S_6$ (M = K, Rb, Cs) that boasts intrinsically large surface areas as well as controllable interfacial electron-transfer as a function of ternary element composition. The pseudo-Chevrel-Phases (PCPs) synthesized in this work are of great interest, as they have strikingly similar compositions and electronic structures compared to their cluster analogues. Unlike their cluster analogues, however, PCPs are comprised of infinite one-dimensional arrays of condensed molybdenum sulfide clusters as is shown in **Figure 1**. These arrays are separated by a metallic intercalant species that affords additional control over electronic structure and will potentially allow for similar control over PCP performance in various types of electronic device components.[20] The ability to intercalate multiple different ternary species into these 1-dimensional materials opens the door for modulation of their anisotropic electrical and optical conductivity,[21] thereby cementing their importance for nano-scale device integration that requires dimensionally controlled components that enable topological charge-transport and spatially resolved exciton separation.[22, 23]

To date, synthetic routes for ternary chalcogenide heterostructure growth are scarce, despite promise of these materials to be integral components in electronic and optical devices.[24] Previous reports of PCP synthesis involve traditional methods of solid state synthesis, including direct synthesis from the constituent elements or from thiomolybdate precursors,[25] as well as ion-exchange from indium-intercalated precursors to form alkali-intercalated PCPs.[25] These methods can be impractically time and energy intensive, and generally do not allow for scalable material production. Herein we report the first instance of a template-free

[a]Department of Chemistry, University of California, Davis, One Shields Avenue, California 95616, United States
[b]Department of Chemical Engineering, University of California, Davis, One Shields Avenue, California 95616, United States

*Correspondence: jevelazquez@ucdavisedu

synthetic route toward nanorod PCPs, wherein rapid microwave heating affords pure-phase, alkali metal-intercalated PCP materials with a high degree of anisotropic crystal growth. To evaluate PCP compatibility with integrated, nano-scale electronic devices which hinges on their unique 1-dimensional electronic properties,[20, 21, 26] in this work capacitive charge storage and inner-sphere electron-transfer properties are evaluated electrochemically as ternary M intercalant composition changes. Investigating electron-transport properties in these chalcogenide materials provides a strong step forward in meeting the contemporary challenge of introducing new functionality in increasingly complex monolithic device schemes.[27]

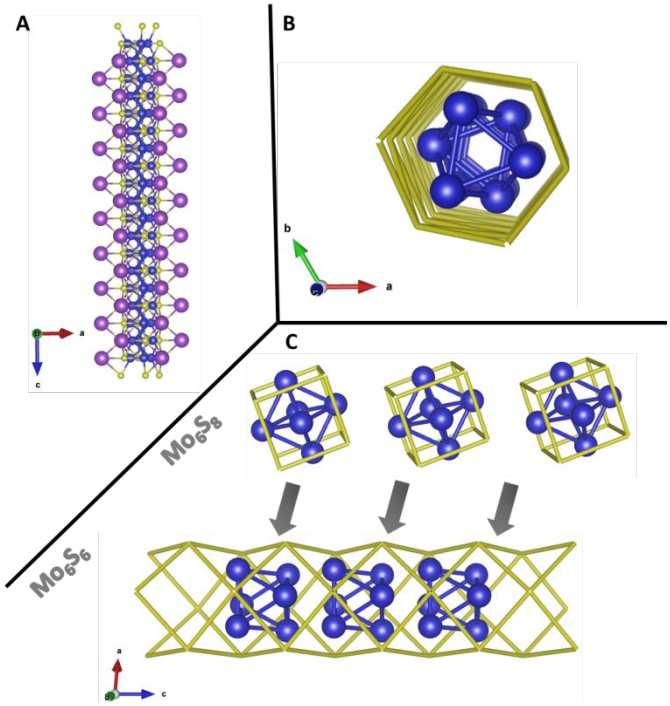

Figure 1. (A) 1-dimensional structure of $M_2Mo_6S_6$ (Alkali = Purple, Mo = Blue, S = Yellow) as viewed perpendicular to the principle hexagonal axis with alkali intercalants surrounding Mo_6S_6 wires, **(B)** Mo_6S_6 wire as viewed along the hexagonal axis, and **(C)** crystal structure representations of the Chevrel parent phase where Mo_6 clusters are significantly separated via S_8 encapsulation, while Mo_6 units form a continuous chain surrounded by an S_6 "sleeve" in the PCP framework.

Experimental

Materials:

Rb (99.999% purity, elemental), Cs (99.999% purity, elemental), MoS_2 (>95% purity, ~325 mesh), and graphite powder (>99% purity, ~125 mesh) were all used as purchased from Alfa Aesar. Mo powder (99.995%, ~250 mesh) and H_2SO_4 were used as purchased from Sigma Aldrich. K_2S (>95%) was used as purchased from Pfaltz and Bauer. Al_2O_3 microfiber was used as purchased from Thermo Fisher Scientific. Fused quartz tubes were purchased from AdValue Technology and blown into round-bottom tubes using an in-house oxyhydrogen torch. Nano-pure H_2O (18.2MΩ) was obtained with an in-house Barnstead E-Pure filtration system.

Synthesis:

All PCPs were synthesized using microwave-assisted solid-state methods described in our previous work.[10, 28] Briefly, stoichiometric amounts of precursors were weighed in a N_2 glovebox according to the balanced reaction

$$2M + 3Mo + 3MoS_2 \rightarrow M_2Mo_6S_6 \quad \textbf{(1)}$$

and ball-milled under N_2 until completely homogenized (~8hrs). Samples were then cold-pressed under N_2 and sealed in 2mm thick quartz round-bottom tubes under tightly packed Al_2O_3 microfiber and graphite as depicted in **Figure S1** to prevent contamination by O_2 during heating. Samples where then removed from the glove box and placed in a graphite bath inside multiple layers of Al_2O_3 insulating foam inside an Ar-filled conventional microwave with inverter technology (Panasonic NN-SN651B) and irradiated at a power of 120-240W for 10 minutes where a temperature of ~750 was held constant. In this reaction, graphite is acting as the microwave susceptor to rapidly yield large amounts of thermal energy.[29] Reactions were immediately quenched in a room temperature water bath.

We note that handling of elemental Cs and Rb precursors can be hazardous even under inert N_2 atmosphere, and significant precautions were taken to ensure any materials introduced to the glove box had been sufficiently dried under vacuum prior to work with the alkalis. Moreover, due to the exothermicity of mixing with sulfide precursors, care was taken to limit batch sizes to <250mg at a time and MoS_2 was used as a precursor rather than elemental S. To further circumvent issues arising from the particularly high exothermicity of mixing Cs with MoS_2, Cs and Mo precursors where first mixed under N_2 prior to addition of MoS_2 and further mixing in order to dilute local concentrations of solid Cs in the ball mill cup. We also note that K_2S can be used as the potassium precursor for K-PCP synthesis owing to its ease of mixing.

Structural and Elemental Characterization:

Crystal phase purity of as-synthesized PCPs was determined via powder X-ray diffraction (PXRD) using Bruker D8 Eco Advance diffractometer with Cu k_α radiation (1.432Å), and powder diffraction patterns were compared with calculated patterns from the Inorganic Crystal Structure Database (ICSD). Experimental lattice parameters were extracted via Pawley refinement using the TOPAS suite from Bruker. High-resolution transmission electron microscopy (HRTEM) was performed using a JEOL JEM-2100F microscope. Morphology of synthesized PCPs was evaluated via scanning electron microscopy (SEM) using a FEI (Hillsboro, Or) Nova NanoSEM 430, while bulk composition was evaluated via energy-dispersive X-ray spectroscopy (EDX) using a FEI Scios Dual Beam FIB/SEM with an Oxford EDX detector.

Electrochemical Characterization:

All electrochemical analyses were performed using a Bio-Logic VSP-300 potentiostat with custom three-electrode cells in an H-shaped

configuration (**Figure S2**) where Ag/AgCl reference electrodes and Pt mesh counter electrodes were used in all cases. Conductive inks of all synthesized PCPs were made by mixing each PCP with conductive carbon black, polytetrafluoroethylene (PTFE) suspension, and isopropyl alcohol. A blank ink was also mixed that contained no PCP. These inks were sonicated for 30 minutes prior to deposition onto conductive carbon substrates. 10µL of each ink was deposited on the bottom half of 1x2cm pieces of conductive, micro-structured Toray carbon paper purchased from Fuel Cell Store, and was then dried under vacuum prior to introduction into an electrochemical cell. This method allowed for us to control the exact mass of PCP that was deposited on each electrode. All experiments herein were performed using 0.5M H_2SO_4 electrolyte in both the working and counter electrode compartments. The electrolyte was de-oxygenated via purging with high-purity Ar for ~30minutes prior to each experiment.

The electrochemically active surface area and specific capacitance of all ink-deposited electrodes were both determined by observing the scan-rate dependence of the capacitive charging current in cyclic voltammetry experiments where scans were centered 0.1V around the open circuit potential, as this was found to be a non-Faradaic region for all of the electrodes.

Resistance to charge transfer was determined via potentiostatic electrochemical impedance spectroscopy (PEIS) with an applied DC bias ranging from -0.3V vs RHE to -0.7V vs RHE and an AC bias with 10mV sinus amplitude ranging from 1MHz-10mHz. Nyquist plots relating imaginary and real components to observable impedance were analyzed with the simplification that interfacial charge-transfer proceeds according to a Randle circuit that involves a capacitive component, a solution/circuit resistance component, and a charge-transfer component. Hence, resistance to charge transfer was taken as the semi-circular diameter of the Nyquist plots.

Hydrogen evolution behavior was observed via linear sweep voltammetry (LSV) where external potential was varied from 0.0V vs RHE down to -1.0V vs RHE for each ink, and current density normalized with respect to surface area is measured. Overpotential was taken as the potential required to achieve a current density of 10mA/cm^2, while Tafel slopes were determined using the linear region of overpotential versus log (current density) plots.

Computational Methods:

Density Funcitonal Theory calculations (as implemented in the Vienna *Ab-initio* Simulation Package (VASP)[30] are used to calculate the surface energies of the relevant $M_2Mo_6S_6$ facets. Initially, the bulk lattice is optimized using the PBE-functional (using 700 eV plane-wave energy cut-off, 4x4x8 K-points);[31] the predicted lattice constants are in good agreement with experimental values. Slab models for the <010>, <110> and <001> facets are used to calculate the surface energy using method of Fiorentini and Methfessel.[32] For these slab calculations, the reciprocal space is sampled using 3x3x1, 6x3x1 and 2x6x1 K-points for <010>, <110> and <001> facets, respectively. All surface calculations are performed using the PBE functional and 520 eV plane-wave energy cut-off. The structures are optimized until the forces on each atom are lower than 0.03 eV/Å. The DFT-optimized bulk and surface structures are available in the Supplementary Information.

Results/Discussion

We have demonstrated that the synthetic method described herein is effective in yielding crystalline $M_2Mo_6S_6$ nanorods as shown in the electron micrographs in **Figure 2a-c**. As shown in **Figure 2d-f**, the PXRD patterns for each PCP are in close agreement with literature, illustrating a hexagonal crystal structure for each PCP. In addition, reaction times using this synthetic method have been reduced to 5-10 minutes owing to rapid conversion of microwave radiation into thermal energy, thereby drastically reducing required energy input in comparison to traditional solid-state methods.[33] Hence this work offers the first account of scalable, template-free, and environmentally benign production of nanostructured Pseudo-Chevrel Phase materials using high-temperature solid-state methods, and indeed represents one of the first known successes in direct solid-state formation of a ternary nanorod material. We speculate that the successful nucleation of these rods can be attributed to one of two potential crystal growth mechanisms: 1) strongly oriented crystal growth may be driven by an insurmountable difference in interfacial energy between "solid" and "liquid" PCP, and the volume energy which results upon changing from liquid to solid phase,[34] or 2) favorable surface free energies for the exposed <010> and <110> facets that drive self-propagating 1-dimensional growth.[35, 36] Density Functional Theory calculated surface energies for the <010>, <110>, and <001> surfaces confirm the latter hypothesis, with the <010> and <110> surfaces exhibiting drastically lower surface energies at ~0.37 eV/formula unit and ~0.93 eV/formula unit, respectively. These surfaces that exist parallel to the observed one-dimensional growth direction are significantly lower than the <001> surface that exhibits a surface energy of ~4.19 eV/formula unit. This is illustrative that surface energy is indeed a strong driving force for the anisotropic nucleation observed for this solid-state reaction. The surfaces of interest can be seen in **Figure S3**, where the <010> (**Figure S3a)** surface clearly requires bisection of fewer bonds than either <110> (**Figure S3b)** or <001> (**Figure S3c)** and yields a more coordinated, more stable interface. The results of this modelling are shown in **Table S1.**

From lattice parameters extracted via Pawley refinement (**Figure S4**) and tabulated in the supporting information in **Table S2**, it is apparent that unit cell parameters for each of the hexagonal PCPs studied here are in good agreement with literature values, with lattice parameters for each of the P63/m (176) structures within 0.19% of expected values.[37] The highest error, belonging to the Cs-PCP, is attributed to the relatively poor R_{WP} of 16.21 that can be ascribed to the lower signal-to-noise ratio in the corresponding diffraction pattern— likely the result of a slightly lower degree of crystallinity. We observe via HRTEM as shown in **Figure S5** that the <010> and <110> facets of Rb-PCP and Cs-PCP are exposed, although no lattice resolution was achieved for K-PCP owing to the increased rod thickness which prevented efficient transmission. Lastly, we do not observe that this method of heating introduces any bulk

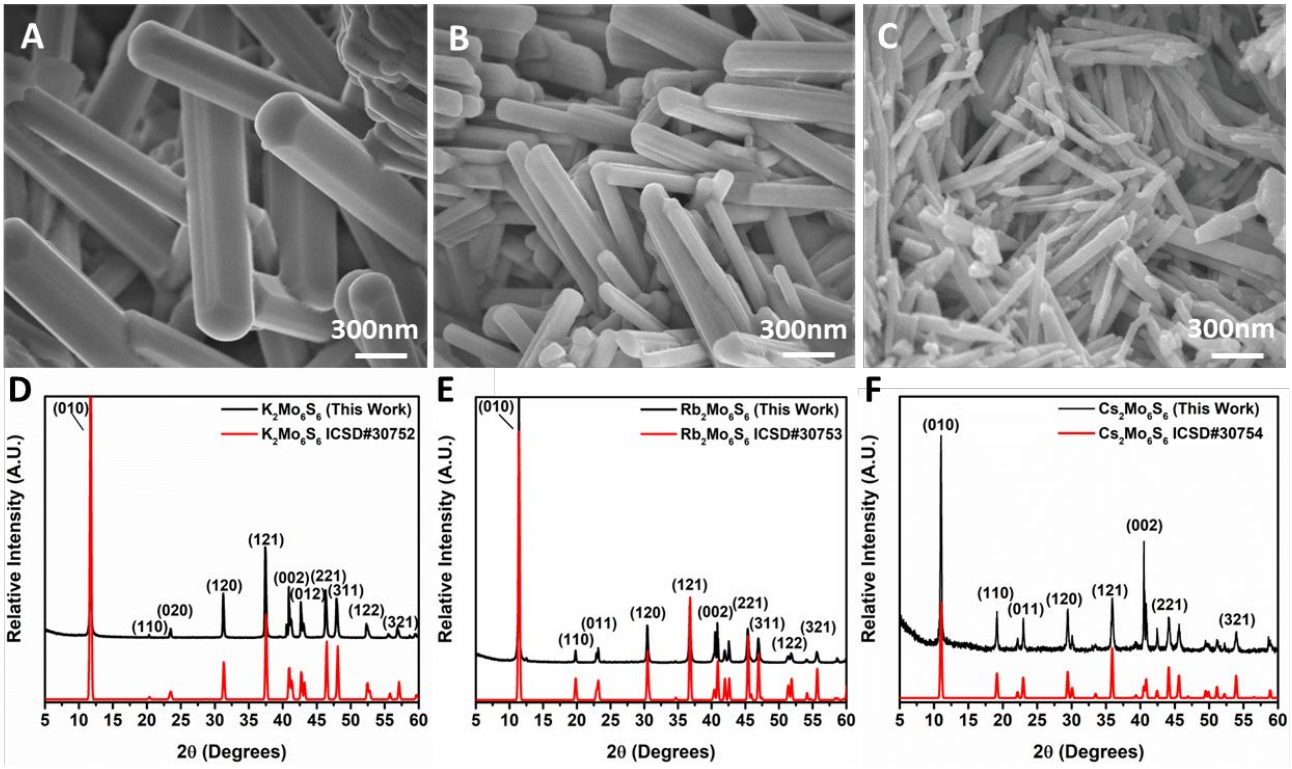

Figure 2. (A)-(C) SEM images for as-synthesized K-PCP (A), Rb-PCP (B), and Cs-PCP (C), **(D)-(F)** Indexed PXRD patterns overlaid with literature patterns from the International Crystal Structure Database (ICSD) for K-PCP (D), Rb-PCP (E), and Cs-PCP (C).

impurity, as evidenced by the EDX point scan spectra in **Figure S6** which indicate the presence of only Mo, S, and each respective alkali metal. Alkali composition was quantified via point scans at three distinct locations on rods of each PCP that were averaged together, yielding atomic percent compositions in a range from 13.12%-15.02%, as would be expected for the $M_2Mo_6S_6$ composition within instrumental error ~1%. To confirm the uniformity of elemental distribution in as-synthesized nanorods, EDX line scans and two-dimensional EDX maps were aquired for isolated rods of each M_2-PCP and the results are shown in **Figures S7-S12**. These scans indicate that alkali metal distribution scales directly with Mo and S distribution in the rods, and there is no obvious deficiency in any constituent element at the tips or along the lenghts of the rods.

In the series of M_2-PCPs, it was found that specific capacity measured via cyclic voltammetry as shown in **Figure S13** and **Figure S14** scaled well with alkali metal electro-positivity (K<Rb<Cs), as Cs-PCP exhibited significantly higher charge storage at 8.45 F/g, compared to Rb and K at 6.34 F/g and 1.48 F/g, respectively (**Figure 3a)**. Indeed, resistance to electrochemical charge transfer determined by EIS as shown in **Figure S16** for the adsorption of H^+ and subsequent reductive evolution of H_2 gas was highest for Cs-PCP at 6.03Ω, followed by Rb and K at 5.88Ω and 4.18Ω, respectively (**Figure 3b**). This indicates that in an electrochemical water splitting device where the reduction half-reaction is given by **Eq. 2**.

$$2H^+_{(aq)} + 2e^- \rightarrow H_{2\,(g)} \qquad \textbf{(2)}$$

K-PCP is likely to be the most efficient material, owing to its lower tendency to resist charge transfer to H^+ to form H_2 (4.18Ω), while Cs-PCP would require unnecessarily high input voltages to maintain comparable rates of H_2 production, due to its higher barrier for inner-sphere electron transfer that is required for proton adsorption. However, the higher resistance to charge transfer for Cs-PCP (6.03Ω) in an electrolyte that is highly conducive to electron transfer is indicative that Cs-PCP can perform well as an aqueous capacitor. This is also in good agreement with the significantly higher specific capacitance (8.45 F/g) for Cs-PCP in comparison to K-PCP (1.48 F/g). In impeding interfacial charge transfer to H^+ in 0.5M H_2SO_4, it can be inferred that Cs-PCP will preferentially mediate alternative small-molecule conversion reactions wherein hydrogen gas evolution is an unwanted side reaction such as CO_2 reduction and N_2 reduction. This speculation warrants further investigation, although we do not explore such a possibility in the present work.

In addition to Nyquist plots that allow for direct extraction of charge-transfer resistance, **Figure S17**and **Figure S18** give the phase angle response and impedance magnitude response for each electrode, respectively, as functions of AC oscillatory frequency. These plots indicate that at mild applied DC bias and low frequency, (log(ω) ~ 0-2) a diffusion-controlled Warburg impedance element exists with a frequency dependence that can be expressed as

$$Z_W = \frac{\sigma(1-j)}{\sqrt{\omega}} \qquad \textbf{(3)}$$

with

$$\sigma = \frac{RT}{n^2F^2A\sqrt{2}}\left(\frac{1}{C^{*O}\sqrt{D_O}} + \frac{1}{C^{*R}\sqrt{D_R}}\right) \qquad \textbf{(4)}$$

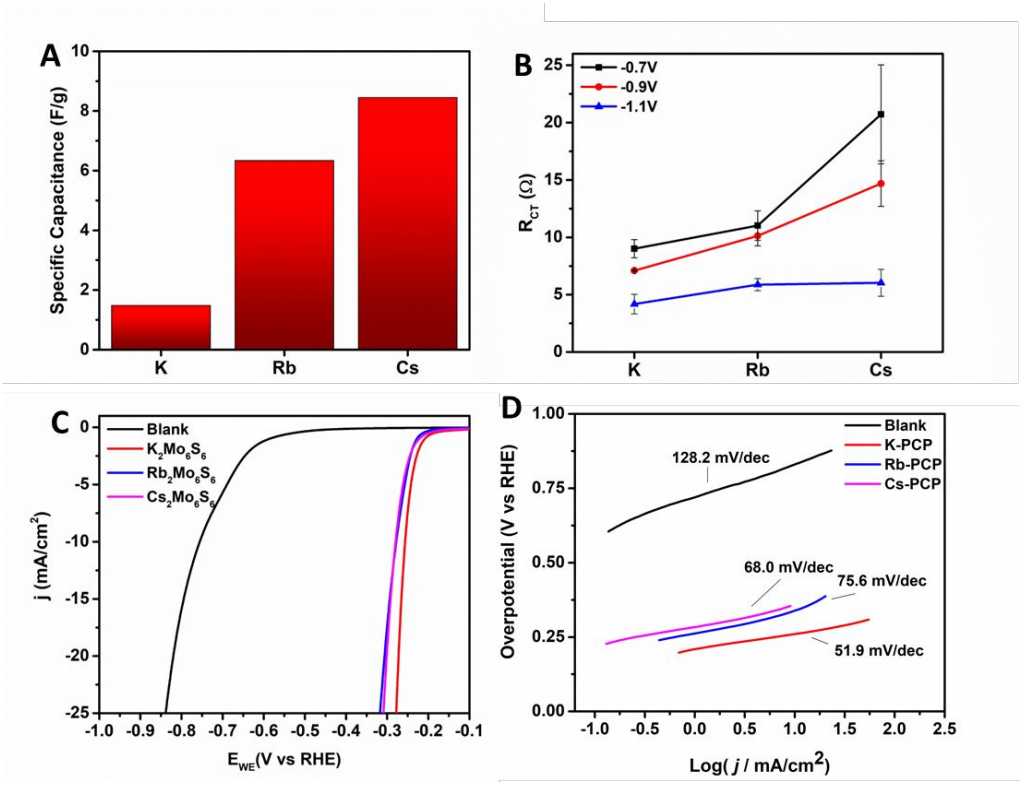

Figure 3. (A) Specific capacitance per gram of M_2PCP, calculated using double layer capacitance and known mass loading onto a conductive carbon substrate, **(B)** Resistance to electron-transfer of M_2PCP inks in a 0.5M H_2SO_4 solution under multiple applied potentials vs RHE, **(C)** Polarization curves obtained via linear sweep voltammetry for M_2PCP inks as well as for a blank ink, all submerged in 0.5M H_2SO_4, and **(D)** Tafel plots for M_2PCP inks along with a blank ink for reference, further illustrating the current-potential response of each ink acting as a catalyst for the Hydrogen Evolution Reaction (HER).

where Z_W is the Warburg impedance, σ is the Warburg coefficient, j is the imaginary term, ω is the radial frequency, C* and D represent concentrations and diffusion coefficients for oxidized and reduced species – H^+ and H_2 in this case—and n represents the number of electrons associated with the electrochemical reaction. We observe from these plots that regardless of applied potential, current response during EIS measurements remains firmly controlled by diffusion for the blank electrode owing to the kinetically hindered electron-transfer that leads to poor mass-transport of H^+ and H_2 to and from the electrode interface, respectively. However, we observe that upon application of an increasingly reductive DC bias, each of the PCP catalyst-loaded electrodes exhibits a drastically reduced impedance modulus at lower oscillatory frequencies, suggesting that neither adsorption/desorption kinetics nor oxidant/reductant diffusion are significantly limiting the observed current response.

In terms of reaction energetics, K-PCP is the most effective catalyst in its class for electrochemical H^+ reduction, as the overpotential required to achieve a current density of 10mA/cm^2 is 270mV, whereas Rb-PCP and Cs-PCP require overpotentials of 349mV and 328mV, respectively, in order to achieve 10mA/cm^2 (**Figure 3c**). While this result of Cs-PCP seemingly outperforming Rb-PCP is surprising owing to the higher charge transfer resistance of Cs-PCP in comparison to its Rb analogue, we note that these overpotential values are very close within experimental error as reported by a single standard deviation in **Figure S19a**, and we do not therefore draw any conclusion that Cs-PCP mediates the HER at significantly milder operating voltages. We observe a strikingly similar trend in Tafel slope which relates applied potential to catalytic current on a logarithmic scale and is a widely accepted descriptor for catalytic activity. As shown in **Figure 3d** and **Figure S19b**, we observe that K-PCP is the most efficient mediator of H^+ reduction, with a shallow Tafel slope of 51.9mV/dec, followed by Rb-PCP and Cs-PCP which exhibit steeper and therefore less desirable Tafel slopes of 75.6mV/dec and 68.0mV/dec, respectively. Again, Rb-PCP and Cs-PCP are similar within experimental error, which may be a result of presently unexplored surface-dependent thermodynamic and kinetic properties such as variable H^+ adsorption strength on sites in different facets of Rb-PCP versus Cs-PCP which can feasibly dictate the overall rate of reaction, although K-PCP is the clear outlier and consequently represents the more promising electrocatalytic composition of all three M_2-PCPs studied.

Conclusions

We have achieved microwave-assisted solid-state synthesis of a ternary nanomaterial without a template or catalyst for anisotropic crystal nucleation. To the best of our knowledge, this is the first of such accounts. We have applied this time- and energy-efficient method to a promising chalcogenide composition wherein alkali metal intercalation can be controlled such that the charge storage

and electron-transfer properties are directly affected. When intercalated by potassium, the 1-dimensional Mo_6S_6 structure readily allows interfacial electron-transfer to electrolytic protons through the hydrogen evolution reaction, while intercalation by Cs leads to a significant increase in charge storage capacity and a resulting high barrier toward charge transfer. In order to deconvolute intrinsic electronic structure versus morphological effects on charge storage capacity, fine control over average nanorod size must likely be coupled with computational and/or spectroscopic evaluation of the composition-dependent $M_2Mo_6S_6$ band structure. A more detailed quantification of the effect of alkali metal electropositivity on electronic structure will ultimately lead to the extraction of useful descriptors for material performance that can be applied to other electronics applications, and this type of elucidation will be a focus of future work related to this family of nanomaterials. For example, quantifying the effect of alkali metal on the currently unknown interfacial kinetics of hydrogen evolution reactivity is an important knowledge gap to address with further systematic evaluation. Further development of composition-structure-function relationships in the expansive transition metal chalcogenide space will elucidate new modalities in controlling charge-transport dynamics and potentially in controlling exciton localization in low-cost, dimensionally reduced, and environmentally benign frameworks.

Conflicts of interest

There are no conflicts to declare.

Acknowledgements

We would like to acknowledge the University of California, Davis for start-up funding for this work, as well as support from the Cottrell Scholar program supported by the Research Corporation for Science Advancement (RCSA Grant ID#26780). JTP would like to acknowledge support from the Chevron fellowship program through UC Davis Institute of Transportation Studies in coordination with Chevron Corporation, as well as support from the Bradford P. Borge fellowship and the Ernest E. Hill Memorial graduate student fellowship. AK acknowledges the computational resources provided by Extreme Science and Engineering Discovery Environment (XSEDE), which is supported by National Science Foundation grant number ACI-1548562.

Notes and references

1. F. Xiong, H. Wang, X. Liu, J. Sun, M. Brongersma, E. Pop and Y. Cui, *Nano Letters*, 2015, **15**, 6777-6784.
2. X. Hong, K. Chan, C. Tsai and J. K. Nørskov, *ACS Catalysis*, 2016, **6**, 4428-4437.
3. D. M. Sim, M. Kim, S. Yim, M.-J. Choi, J. Choi, S. Yoo and Y. S. Jung, *ACS Nano*, 2015, **9**, 12115-12123.
4. A. A. Tedstone, D. J. Lewis and P. O'Brien, *Chemistry of Materials*, 2016, **28**, 1965-1974.
5. Y. Gong, J. Lin, X. Wang, G. Shi, S. Lei, Z. Lin, X. Zou, G. Ye, R. Vajtai, B. I. Yakobson, H. Terrones, M. Terrones, Beng K. Tay, J. Lou, S. T. Pantelides, Z. Liu, W. Zhou and P. M. Ajayan, *Nature Materials*, 2014, **13**, 1135.
6. Y. Jung, Y. Zhou and J. J. Cha, *Inorganic Chemistry Frontiers*, 2016, **3**, 452-463.
7. J. Etzkorn, H. A. Therese, F. Rocker, N. Zink, U. Kolb and W. Tremel, *Advanced Materials*, 2005, **17**, 2372-2375.
8. A. Splendiani, L. Sun, Y. Zhang, T. Li, J. Kim, C.-Y. Chim, G. Galli and F. Wang, *Nano Letters*, 2010, **10**, 1271-1275.
9. A. Ramasubramaniam, D. Naveh and E. Towe, *Physical Review B*, 2011, **84**, 205325.
10. J. T. Perryman, J. C. Ortiz-Rodríguez, J. W. Jude, F. P. Hyler, R. C. Davis, A. Mehta, A. R. Kulkarni, C. J. Patridge and J. M. Velázquez, *Materials Horizons*, 2020, **7**, 193-202.
11. J. Jun, G. Minrui, S. Wenchao and Y. Yushan, *Angewandte Chemie International Edition*, 2016, **55**, 15240-15245.
12. P. Liu, Y. Choi, Y. Yang and M. G. White, *J Phys Chem A*, 2010, **114**, 3888-3895.
13. C. Liu and P. Liu, *ACS Catalysis*, 2015, **5**, 1004-1012.
14. G. Gershinsky, O. Haik, G. Salitra, J. Grinblat, E. Levi, G. Daniel Nessim, E. Zinigrad and D. Aurbach, *Journal of Solid State Chemistry*, 2012, **188**, 50-58.
15. E. Levi, Y. Gofer, Y. Vestfreed, E. Lancry and D. Aurbach, *Chemistry of Materials*, 2002, **14**, 2767-2773.
16. P. Canepa, G. Sai Gautam, D. C. Hannah, R. Malik, M. Liu, K. G. Gallagher, K. A. Persson and G. Ceder, *Chemical Reviews*, 2017, **117**, 4287-4341.
17. R. C. a. M. Sergent, *Superconductivity in Ternary Compounds I*, Springer-Verlag Berlin Heidelberg, 1982.
18. Ø. Fischer, *Applied physics*, 1978, **16**, 1-28.
19. T. Caillat, J. P. Fleurial and G. J. Snyder, *Solid State Sciences*, 1999, **1**, 535-544.
20. J. Kibsgaard, A. Tuxen, M. Levisen, E. Lægsgaard, S. Gemming, G. Seifert, J. V. Lauritsen and F. Besenbacher, *Nano Letters*, 2008, **8**, 3928-3931.
21. I. Vilfan, *The European Physical Journal B - Condensed Matter and Complex Systems*, 2006, **51**, 277-284.
22. R. Ge, X. Wu, M. Kim, J. Shi, S. Sonde, L. Tao, Y. Zhang, J. C. Lee and D. Akinwande, *Nano Letters*, 2018, **18**, 434-441.
23. F. F. Wang, X. Y. Hu, X. X. Niu, J. Y. Xie, S. S. Chu and Q. H. Gong, *Journal of Materials Chemistry C*, 2018, **6**, 924-941.
24. K. Galatsis, P. Gargini, T. Hiramoto, D. Beernaert, R. DeKeersmaecker, J. Pelka and L. Pfitzner, *IEEE Technology and Society Magazine*, 2015, **34**, 21-30.
25. M. Potel, R. Chevrel, M. Sergent, J. C. Armici, M. Decroux and Ø. Fischer, *Journal of Solid State Chemistry*, 1980, **35**, 286-290.
26. S. Kasap, C. Koughia and H. E. Ruda, in *Springer Handbook of Electronic and Photonic Materials*, eds. S. Kasap and P. Capper, Springer International Publishing, Cham, 2017, DOI: 10.1007/978-3-319-48933-9_2, pp. 1-1.
27. L. Greene, T. O. M. Lubensky, M. Tirrell, P. Chaikin, H. Ding, K. Faber, P. Hammond, C. Heckle, K. Hemker, J. Heremans, B. Jones, N. Mason, T. Mason, T. Shahnaz Rahman, E. Reichmanis, J. Sarrao, S. Sinnott, S. Stemmer, S. Stupp, T. I. A. Benson Tolle, M. Weaver, T. Younkin and S. Zinkle, *Frontiers of Materials Research: A Decadal Survey*, United States, 2019.
28. J. T. Perryman, F. P. Hyler, J. C. Ortiz-Rodríguez, A. Mehta, A. R. Kulkarni and J. M. Velázquez, *Journal of Coordination Chemistry*, 2019, **72**, 1322-1335.

29. S. Chandrasekaran, T. Basak and R. Srinivasan, *International Communications in Heat and Mass Transfer*, 2013, **48**, 22-27.
30. J. Hafner, *Journal of Computational Chemistry*, 2008, **29**, 2044-2078.
31. J. P. Perdew, K. Burke and M. Ernzerhof, *Physical Review Letters*, 1997, **78**, 1396-1396.
32. V. Fiorentini and M. Methfessel, *Journal of Physics: Condensed Matter*, 1996, **8**, 6525-6529.
33. E. E. Levin, J. H. Grebenkemper, T. M. Pollock and R. Seshadri, *Chemistry of Materials*, 2019, **31**, 7151-7159.
34. A. Mariaux and M. Rappaz, *Acta Materialia*, 2011, **59**, 927-933.
35. S. J. Jung, T. Lutz, M. Boese, J. D. Holmes and J. J. Boland, *Nano Letters*, 2011, **11**, 1294-1299.
36. C. J. O'Kelly, S. J. Jung and J. J. Boland, *Crystal Growth & Design*, 2016, **16**, 7318-7324.
37. *Inorganic Crystal Structure Database (ICSD) https://www.fiz-karlsruhe.de/*

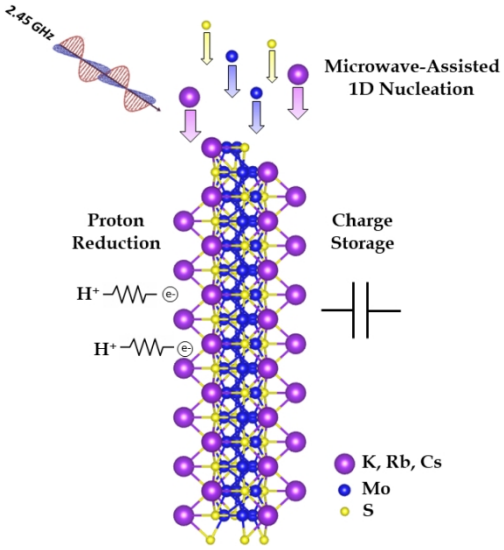

338x190mm (96 x 96 DPI)